Reconfigurable Dual-Band Capsule-Conformal Antenna Array for In-Body Bioelectronics

Denys Nikolayev, Anja K Skrivervik, John S Ho, Maxim Zhadobov, Ronan Sauleau

Reconfigurable Dual-Band Capsule-Conformal Antenna Array for In-Body Bioelectronics

Denys Nikolayev, *Member, IEEE,* Anja K. Skrivervik, John S. Ho, *Member, IEEE,* Maxim Zhadobov, *Senior Member, IEEE,* and Ronan Sauleau, *Fellow, IEEE*

***Abstract*—Wireless in-body bioelectronics offer powerful biosensing and therapeutic capabilities. Efficient and robust in-body antenna designs are required to ensure a reliable through-body link, increase data rates, and reduce power budgets. This study proposes and demonstrates a pattern- and frequency-reconfigurable capsule-conformal antenna array that responds to the challenges of next generation in-body bioelectronics. The array comprises two mirrored dual-band elements operating at 434-MHz and 2.45-GHz ISM bands. Tissue-matched dielectric loading of the array improves the radiation efficiency and ensures quasi tissue-independent operation for both bands. Owing to the full ground plane, the antenna is shielded from the capsule payload. The achieved efficiencies are compared to the fundamental limitations and closely approach them. The realized gains are –28.9 dBi and –18.6 dBi at 434 MHz and 2.45 GHz, respectively, when the array is placed in the center of a ⌀100-mm diameter spherical phantom with muscle-equivalent properties. Using a single switch, the array can be reconfigured to adjust the angular position of the nulls in the radiation pattern in both bands thereby enabling synthesis of an effectively null-free omnidirectional pattern. The array prototypes are fabricated, and the impedance and far-field radiation patterns are characterized to validate the design in tissue-equivalent liquid phantoms.**

***Index Terms*—bioelectronics, biomedical telemetry, conformal array, dual-band antenna, implantable, in-body, ingestible, microstrip antenna, reconfigurable antenna, robustness.**

I. Introduction

WIRELESS implantable, ingestible and injectable (in-body) bioelectronics offer powerful capabilities for medicine, clinical research, and fundamental science to continuously monitor physiological processes [1], [2]. Implantable neural interfaces allow us to interact with central and peripheral nervous systems *via* mapping, assisting, augmenting, and repairing cognitive or sensory-motor functions [3]. The emerging concept of electroceuticals envisions targeting peripheral nerves with miniaturized wireless devices in order to control organ functions with greater efficacy and fewer side effects than drugs [4]. The last decade has seen tremendous cross-disciplinary progress in μm-scale biosensors and actuators, biomaterials and bio-inspired systems, neuroengineering, bioinformatics, and machine learning. Integrating of these technologies into the next generation of in-body bioelectronics requires at least two fundamental challenges to be overcome: 1) efficient, reliable, and safe wireless communication and 2) adequate powering that relies on either batteries that hinder the miniaturization, hazardous percutaneous links, or wireless energy transfer [5].

To address these challenges, significant effort has been devoted to the design of in-body antennas that enable a power-efficient interface with the external world [6]–[27]. However, a typical radiation efficiency of an in-body antenna remains very low (0.1–1%) because of electromagnetic (EM) losses associated with the human body. Given an average input power of $\sim$ 10 dBm, increasing the off-body radiated power remains a major challenge. Fundamental bounds on the radiation efficiency can be established for simple models of the human body as a function of the antenna size, type, operating frequency, position and orientation in a body—a highly lossy and heterogeneous medium [30]. Based on *a priori* knowledge of the antenna size and its approximate depth in tissues (from the device specifications), the optimal antenna type, operating frequency, and achievable efficiency can be evaluated using theoretical models in [31], [32]. These analyses reveal that the optimal frequency varies significantly with the depth of the device (from $\sim$ 100 MHz to a few GHz), and that the placement and orientation of the antenna has a major effect on the radiation efficiency. However, in real-world applications, the exact position and orientation of the device are hard to control (especially, for ingestibles). Only rotation can account for $\sim$ 10 dB variation in path loss [28], [29]. As such, the ability to reconfigure both the operating frequency as well as the radiation pattern is critical to maintain near-optimal performance under varying conditions. This can be achieved in part using dual- or multi-band antennas [18]–[26]. This feature can also be used to multiplex the antenna role to both data transceiver and a power receiver [18]. Finally, to mitigate the uncertainly of the device orientation, an in-body radiation pattern reconfigurability is a promising approach [27].

In this paper, we propose and demonstrate a first capsule-conformal antenna array in which both the operating frequency and the radiation pattern can be reconfigured to achieve near-optimal radiation performance across a broad range of conditions. To accomplish this, a novel mirror-symmetric conformal array of two dual-band microstrip-antenna elements was synthesized. Tissue-matched dielectric loading is employed to increase the radiation efficiency, improve the impedance robustness against the variation of tissue EM properties, and

Manuscript received March 11, 2021, revised November 4, 2021, and accepted November 18, 2021.

This work was supported by the French region of Brittany through the SAD "EM-NEURO." *(Corresponding author: Denys Nikolayev, d@deniq.com)*

D. Nikolayev, M. Zhadobov, and R. Sauleau are with the Univ Rennes, CNRS, IETR – UMR 6164, FR-35000 Rennes, France.

A. K. Skrivervik is with the Microwave and Antenna Group (MAG), École Polytechnique Fédérale de Lausanne, CH-1015 Lausanne, Switzerland.

J. S. Ho is with the Department of Electrical and Computer Engineering, Institute for Health Innovation and Technology, Singapore, and also with the N.1 Institute, National University of Singapore, Singapore.

reduce the specific absorption rate (SAR) for both bands. A single switch is used to reconfigure the radiation patterns in both bands thereby providing an effective null-free pattern. Finally, the antenna array is fully backed by a ground plane and therefore well shielded from the capsule payload.

This paper is organized as follows. Section II addresses the theoretical preliminaries as well as the antenna miniaturization and synthesis approaches and its operating principle. Section III deals with the optimization and numerical analysis of the antenna performance. Section IV provides the experimental validation. Conclusions are drawn in Section V.

II. Antenna Concept and Design

A. Theoretical Considerations

Both the maximum achievable radiation efficiency $\eta_{\text{idl}}(f)$ and the optimal operating frequency $f_{\text{opt}}[\max(\eta_{\text{idl}})]$ of an in-body antenna strongly depend on its dimensions and depth in the tissues [31], [32]. For clinically relevant depths (1–10 cm) and antenna dimensions (centimeter-scale), the optimal operating frequency range is within approx. 0.3–3 GHz range [31]. Therefore, to enable efficient operation for both shallow and deep-body implantation, two ISM (Industrial, Scientific and Medical) bands were chosen: $f_1 = 434$ MHz and $f_2 = 2.45$ GHz.

Prior work on in-body antennas has largely focused on magnetic-type antennas to avoid the high dielectric losses associated with tissues. Recent theoretical studies, however, have shown that electric-type antennas can counterintuitively achieve higher radiation efficiencies at f_{opt} than the magnetic ones [31]. At first glance, it may seem illogical as body tissues are in general electrically lossy and nonmagnetic. However, the electric antennas benefit significantly from the dielectric loading by neighboring tissues, which increases their effective aperture by a factor up to $\sqrt{\varepsilon_{r,\text{tissue}}}$ [34]. For instance, considering the muscle tissue at 434 MHz ($\varepsilon_r = 56.9$), this is a factor of 7.5.

Seeing this, we should not be surprised to find that low-permittivity plastic capsule shells reduce the effective ε_r in the region of the antenna near field and therefore suppress the effect of dielectric loading. Conversely, equalling the permittivity of the shell with the tissue improves the wave-impedance matching between the antenna and its operating environment and significantly enhances the radiation performance [33]. To further leverage this effect, we favor a shell material with its permittivity close to the maximum among different tissues ($\varepsilon_r \approx 80$ at 434 MHz [35]). Due to the antenna having a ground plane, the near field circulates primarily outside of the cylindrical antenna surface. This zone comprises the capsule shell and the surrounding tissue. Given that the imaginary part ε'' of the shell is lower than that of the surrounding tissues, the near field losses of electric-type antennas (function of ε'') are mitigated.

Among electric antenna types, we choose to synthesize a microstrip-based design since its integral ground plane would help to decouple the conformal-capsule antenna (as shown in Fig. 1a) from the inner components of the device: batteries, biosensors, integrated circuits, and so on. This has a double benefit of 1) reducing the risk of antenna-induced EM interference with the device and 2) making the antenna performance independent of the capsule components therefore improving its versatility.

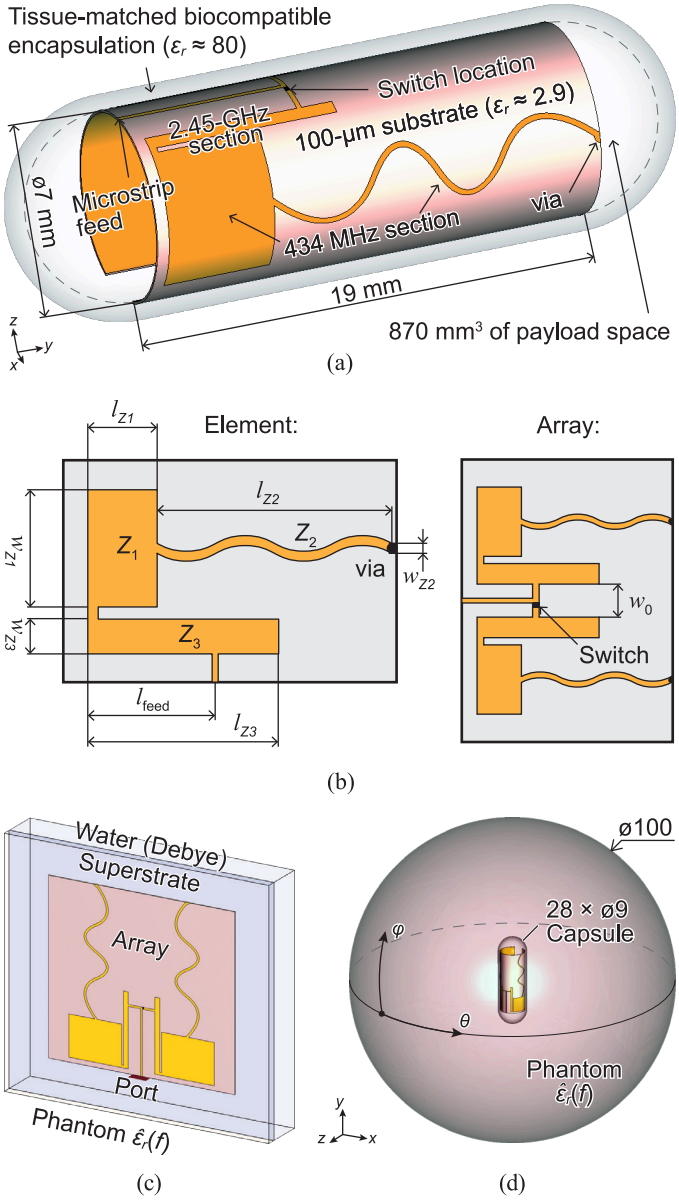

Fig. 1. Antenna concept and design (units: millimeters). (a) Overview of the proposed in-body antenna conformal to the inner surface of a 28×ø9 in-body capsule. (b) Planar geometry of the proposed antenna element and a reflection-symmetric array (not to scale). Optimized parameters: $w_{Z1} = 6.7, l_{Z1} = 4.5, w_{Z2} = 0.23, l_{Z2} = 13.5, w_{Z3} = 0.548, l_{Z3} = 8.1, l_{\text{feed}} = 6.5, w_0 = 3$. (c, d) Simulation setups in CST Studio Suite: (c) planar model used for rapid antenna optimization (TD solver) and (d) conformal model in a ø100 spherical phantom (FD solver).

Beyond its material and geometry, the input impedance of an in-body antenna also strongly depends on the effective EM properties of the medium in its near-field zone. In case of biological tissues, these properties vary as $\varepsilon_r \in [10..80], \sigma \in [0..2.4]$ S·m^{-1} at 434 MHz and $\varepsilon_r \in [5..70], \sigma \in [0..3.5]$ S·m^{-1} at 2.45 GHz [35]. Fat tissue defines the lower limit of ε_r, whereas the upper limit is determined by the high-

water-content body fluids such as a cerebrospinal, bile, or a gastric fluid. The variation of tissue EM properties detunes the antenna reducing its total efficiency $\eta_{\text{tot}} = \eta(1 - |\Gamma|^2)$, where Γ is the antenna reflection coefficient. As the majority of in-body applications require operating from soft water-based tissues ($\varepsilon_r \sim 50$), a common practice in literature is to optimize the antenna in terms of $|S_{11}|$ in a muscle-equivalent environment ($\varepsilon_r = 56.9, \sigma = 0.8$ S·m^{-1} at 434 MHz and $\varepsilon_r = 52.7, \sigma = 1.7$ S·m^{-1} at 2.45 GHz) [2]. Finally, the ability of the antenna to remain well-matched in a wide range of tissues characterizes its robustness. Again, tissue-matched high-permittivity shells come in handy as they reduce the variation of effective EM properties in the near field [9].

B. Miniaturization, Synthesis, and Operating Principle

The antenna array is designed to conform to the inner surface of a capsule shell; the dimensions of the capsule are 28 mm $\times\varnothing$9 mm. The overall structure of the antenna consists of two microstrip sections (Fig. 1a): a 434-MHz one comprising the elements Z_1 and Z_2 (Fig. 1b) and a 2.45-GHz one (Z_3 element). Miniaturization is required for the 434-MHz antenna section ($\lambda_0/2 \approx 34$ cm) to fit on the 19-mm-long substrate (Fig. 1a). It was achieved using: 1) dielectric loading by the tissues and superstrate, 2) shorting of the antenna element using a via (Fig. 1b), 3) introducing a characteristic-impedance (Z_c) step from low-Z_1 to high-Z_2 (Fig. 1b), and 4) meandering the Z_2 section to increase its electric length. For the 2.45-GHz section ($\lambda_0/2 \approx 6$ cm), the miniaturization is attained using the dielectric loading.

The antenna is synthesized on a 101.6-μm-thick substrate backed with a full ground plane (Rogers ULTRALAM 3850HT: liquid crystal polymer, $\varepsilon_r = 2.9, \tan\delta = 0.002$). Fig. 1b shows the geometry and dimensions of the antenna element and of the array. The rectangular microstrip Z_1 (low Z_c) links to both Z_2 (high Z_c) and Z_3 microstrip sections (2.45-GHz section). The Z_2 element is connected to Z_1 on one side and short-circuited to the ground plane using a via on the other. Z_2 is meandered to increase its electric length to achieve the first antenna resonance at 434 MHz. Z_3 connects to Z_1 using a short microstrip transition. The feed connects to the longer (non-radiating) edge of Z_3 at the distance l_{feed} from the reference plane of the antenna.

The resonance frequencies and impedance of the antenna depend on the dimensions of Z_1, Z_2, and Z_3. Specifically, by varying the widths w_{Z_1} and w_{Z_2} and the ratio of their length l_{Z_2}/l_{Z_1} while keeping the overall antenna length $l_{Z_1} + l_{Z_2} = \text{const}$, we can adjust the first resonant frequency f_1 as well as match the antenna to a given impedance at f_1 (e.g., 50 Ω). The second resonance frequency f_2 is inversely proportional to the length l_{Z_3}. The input impedance at f_2 depends on the width w_{Z_3} and the feed location l_{feed}. In this way, the approximate dimensions of the antenna can be derived using the transmission-line model [38, Ch. 14].

The design of Z_1 and Z_2 together define the first resonance frequency according to the transmission line expression through the ratio of impedances Z_n and electrical lengths $l_{Z_n}\beta_{Z_n}$ as $-Z_1 + Z_2 \tan(\beta_{Z_2} l_{Z_2}) \tan(\beta_{Z_1} l_{Z_1}) = 0$, where

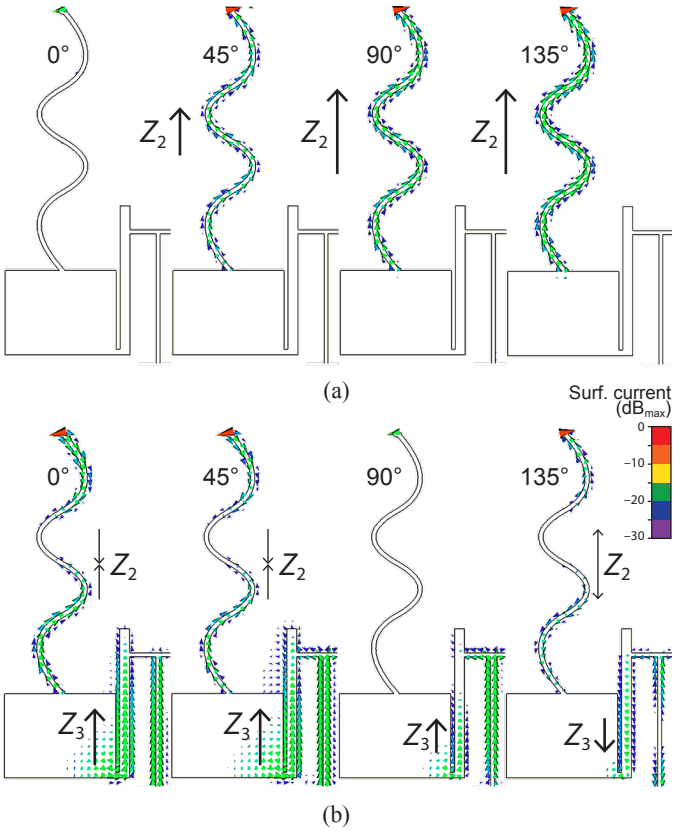

Fig. 2. Surface current distributions on the radiating element (half of the array is shown owing to the symmetry) at two operating frequencies and different phases: (a) 434 MHz (radiating currents in Z_2) and (b) 2.45 GHz (radiating currents in Z_3).

$\beta_{Z_n} = 2\pi f\sqrt{(\varepsilon_{r,\text{eff}})}/c$ is the phase constant and $n = 1, 2$ [36, p. 59], [37]. Clearly, the resonance at 434 MHz can be achieved with an infinite number of $\{Z_1, Z_2, l_{Z_1}, l_{Z_2}\}$ combinations. However, achieving simultaneous operation at 2.45 GHz puts an implicit constraint on these values that will be accounted for during the antenna optimization (Section III). To initialize the dimensions $\{l_{Z_3}, w_{Z_3}\}$ prior to the optimization, the second resonance frequency can be roughly predicted using a quarter-wave patch antenna model [38, Ch. 14]. In order to obtain the values of Z_n and β_{Z_n} that take into account the heterogeneous environment of the antenna (the substrate, shell, and tissues), we used a reduced-order numerical model proposed in [39]. The predicted length $\lambda/4 = 8.18$ mm (based on the estimated effective $\varepsilon_r \approx 14$) agrees well with post-optimization value $l_{Z3} = 8.1$ mm.

Fig. 2 shows the surface current distributions at two operating frequencies. The 434-MHz section radiates as a quarter-wave microstrip antenna. Prominent E-plane-aligned current flows in the Z_2 section (Fig. 2a) with its maximum on the edge where the via short-circuits Z_2. At 2.45 GHz, the radiation primarily comes from the co-aligned currents in Z_3 with an in-phase contribution from the feed line (Fig. 2b). Another (unintentional) resonance occurs in Z_2: two opposite currents meet at the middle of the section. In contrast to the distribution at 434 MHz, these currents cancel each other out and do not contribute to the radiation."

The resulting antenna design has several features that are advantageous for full utilization of the capsule surface. First, its length (i.e., along the E-plane) can span over the entire available surface of the substrate increasing therefore the effective aperture. Second, the synthesized antenna can be relatively narrow. This, along with the location of the feed point at the side of Z_3, allows us to form an array of two mirror-symmetric antenna elements as shown in Fig. 1b. Such a configuration will also have the y–z plane symmetry in its radiation pattern in contrast to the asymmetric single antenna element. By switching the antenna state between the array and single-element, a pattern reconfigurability can be realized to avoid deep nulls in the antenna radiation. This can be achieved by placing a miniature RF switch at the location of the feed branching (Fig. 1a, b). When this switch is closed (i.e., in "on" state), the antenna operates in the array mode with yz-plane-symmetric radiation pattern. When open ("off" state), only one element is active, which breaks the symmetry of the radiating structure. As the result, the null of the radiation pattern can be rotated (Section III-B). In the single-element mode, the passive element is short-circuited to the ground plane, that reduces its coupling to the active one.

Although addition of the switch increases the system complexity, the feasibility of even more complex approach was successfully demonstrated in [27] where two MOSFETs have been implemented into a reconfigurable capsule-conformal antenna prototype. Moreover, as demonstrated in [16], a single-layer conformal PCB can host several RF components routed individually to the implant circuitry *via* printed conductors.

From the power budget perspective, a miniature CMOS switch has a typical current consumption of about 1 μA. Given a 3 V potential, its power consumption is about -25 dBm, which is negligible in comparison to the $\sim 10..20$ dBm power consumed by the antenna. Operating a switch is therefore justifiable to improve the radiated power around the null directions of the antenna by about 1–10 dB.

C. Choosing the Phantom Shape

Let us now take a closer look at the evaluation of radiation performance of in-body antennas. The conventional definition for the radiation pattern fails in the case of radiation into a lossy medium as the antenna diagram strongly depends upon the origin of coordinates [40]. Therefore, the far-field analysis assumes instead the radiation of the entire phantom in free space. Individual body morphologies vary significantly, and the antenna radiation performance cannot be decorrelated from these factors [32]. Analyzing the antenna in a realistic anatomical phantom is therefore impractical in most cases. Since the results depend strongly on the exact location and orientation of the device in a given tissue, it impairs the reproducibility of the results and makes it very difficult to accurately compare the radiation performance of various designs reported in literature. For these reasons, and seeing the increased computational cost of anatomical phantoms, the latter should be reserved for the analysis of special cases where a homogeneous model will fail to demonstrate a given feature or effect.

The results obtained using a simple well-characterized phantom are reproducible and give more insight into the intrinsic radiation of the antenna. Different designs can be gauged relatively to the maximum achievable efficiency derived for this reference phantom [31], [32]. Specifically, the propagation and reflection losses induced by the phantom can be decorrelated from the intrinsic antenna losses (i.e., near field and conductor) in this approach. The phantom shape choice therefore does not play a significant role in this analysis since the same propagation and reflection losses are accounted for in both the theoretical source and the realistic antenna models. A sphere (Fig. 1d) is a good candidate for a standard phantom. This shape introduces isotropic direction-independent losses conserving the intrinsic antenna pattern (any other shape will introduce anisotropic losses). A spherical symmetry helps in constructing computationally efficient theoretical models, e.g., using a spherical wave expansion approach [32] or a 2D-axisymmetric full-wave one [31]. Finally, the radiation performance computed in a simple phantom is highly reproducible and is relatively easy to verify experimentally.

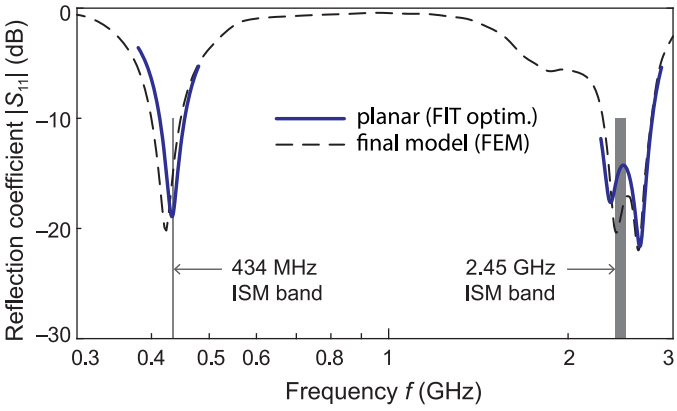

Fig. 3. Comparison of the reflection coefficient $|S_{11}|$ computed using the rapid planar FIT model (used for the optimization, Fig. 1c) and the accurate conformal FEM model (Fig. 1d).

III. Numerical Analysis and Optimization

We used CST Studio Suite 2021 [41] (CST) to analyze and optimize the proposed antenna. The initial dimensions were obtained using the analytical expressions given in Section II-B. On the one hand, this theoretical model accurately predicts resonance frequencies of the antenna element. On the other, ensuring the 50Ω-impedance matching for both operation states (i.e., in the single-element and array modes) while taking into account the mutual coupling between two elements in the array configuration and high interaction between the antenna parameters required optimization. To satisfy $|S_{11}| \leq -10$ dBi for both bands, seven geometrical variables were fine-tuned with a constraint $l_{Z_1} + l_{Z_2} = \text{const}$. Clearly, such optimization would be too computationally expensive if approached directly as given in Fig. 1d.

A better approach to optimization is to employ rapid hardware-accelerated codes such as a Finite Integration Technique (FIT) implemented in the CST time-domain (TD) solver. Considering the orthogonal hexahedral mesh required for FIT, a planar antenna model approximation was used (Fig. 1c) to reduce the computational costs. In this model, an infinite

[i.e., extending into the perfectly matched layer, (PML)] lossy muscle-equivalent phantom surrounds the antenna. The antenna is covered with a superstrate and backed by pure water (EM properties modeled using Debye relaxation). Zero-thickness impedance boundaries modeled top and bottom conductive layers of the antenna (copper, $\sigma = 5.96 \times 10^7$ S·m^{-1}). The solution mesh was defined using an adaptive refinement with $\delta|S_{11}|\,[f = 2.45\ (\mathrm{GHz})] < 1\%$ for two consecutive passes. Finally, the mesh adaptive refinement was switched to the CST *expert-based system* adaptivity mode to speed-up the computation. Further reduction of the total optimization time was achieved by: 1) hardware acceleration using NVIDIA Tesla K20c GPUs and 2) parallelization of the the Trust Region Framework algorithm over seven computational nodes (number of nodes equals the number of parameters to optimize).

The optimized conformal-antenna model (Fig. 1d) was analyzed using the frequency domain solver (FD) of CST [finite element method (FEM)]. The FEM mesh was refined adaptively until two criteria were reached simultaneously: 1) the reflection coefficient error $\delta|S_{11}\,(f_1, f_2)\,| < 1\%$ for three consecutive passes and 2) the maximum gain error $\delta \max\,[G\,(f_1, f_2)] < 1\%$ for two consecutive passes. PML truncated the model at the distance $\lambda/2$ at 434 MHz. Fig. 3 compares the accuracy of the FEM model in terms of $|S_{11}|$ with the rapid FIT model used for the optimization.

A. Impedance Performance

The impedance performance of the antenna in the array and single element configurations is compared in Fig. 4. The results were computed in the phantom with dispersive muscle-equivalent EM properties [35] (if not explicitly stated otherwise, all values hereafter are reported for a muscle-equivalent environment). The antenna shows a single resonant frequency [i.e., when $\mathbb{I}\mathrm{m}\,(Z_{\mathrm{in}}) = 0$] around the 434 MHz band and a double resonance around 2.45 GHz band.

In the single-element mode, the coupling between the active and passive elements can be determined by placing an additional port at the switch location. This analysis yields $|S_{21}| = -75$ dB for the 434-MHz band and $|S_{21}| \in [-65, -68]$ dB for the 2.45-GHz band.

Although the antenna operates below $|S_{11}| < -10$ dB in both modes, the array configuration shows a marginally better performance as well as lower SAR (Table I). Therefore, we define it as a default operating mode of the antenna and provide further impedance results only for the array configuration for brevity.

Fig. 5 shows the impedance characteristics of the array as a function of surrounding tissues. For the muscle, the bandwidth values are 42 MHz (10%) and 535 MHz (22%) for the 434 MHz and 2.45 GHz bands, respectively. The impedance of in-body antennas is sensitive to the EM properties of adjacent tissues as well as to the device components as batteries, sensors, etc. A robust design is such that remains operational in a wide range of tissue EM properties. In addition, decoupling the antenna from the device components presents the following advantages: versatility of the antenna (can be used "as is" with a wide range of biomedical circuits and sensors), ease of the antenna integration, and mitigation of the EM interference between the antenna and the device circuits.

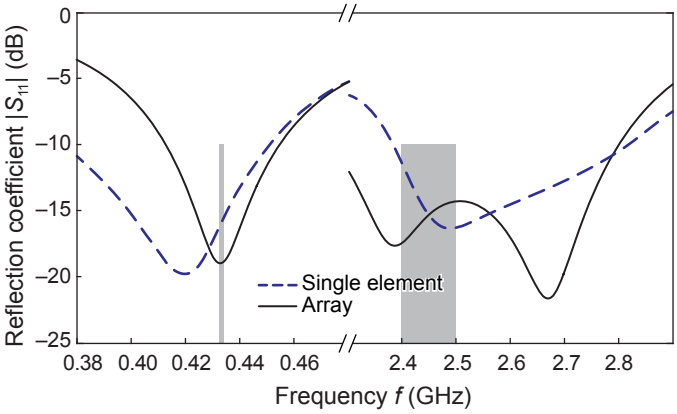

Fig. 4. Comparison of the reflection coefficients $|S_{11}|$ of the antenna in array and single element configurations.

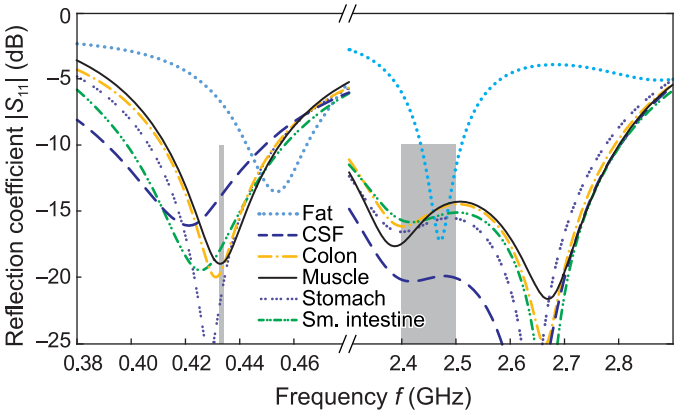

Fig. 5. Reflection coefficient $|S_{11}|$ computed in different tissues.

1) Robustness to Tissue: To study the detuning immunity range within different tissues, we analyzed its reflection coefficient $|S_{11}|$ at both operating frequencies in a phantom parametrized to cover the entire range of tissue EM properties: from averaged fat to cerebrospinal fluid [35]. Specifically, the following ranges were analyzed: $\varepsilon_r \in [10..80]\,, \sigma \in [0..2.4]$ S·m^{-1} at 434 MHz and $\varepsilon_r \in [5..70]\,, \sigma \in [0..3.5]$ S·m^{-1} at 2.45 GHz. Eleven values were computed for each range, the step size was $\Delta\varepsilon_r = 7, \Delta\sigma = 0.23$ for 434 MHz and $\Delta\varepsilon_r = 5.5, \Delta\sigma = 0.35$ for 2.45 GHz. Fig. 6 depicts the detuning immunity of the proposed antenna. It remains well matched (i.e. $|S_{11}| < -10$ dB) for most tissues except for the fat where $|S_{11}| \approx -7$ dB at 434 MHz and 2.40 GHz (yet, $|S_{11}| < -10$ dB at 2.43–2.5 GHz).

2) Robustness to Capsule Components: Microstrip-based designs help achieving robustness as a ground plane shields the antenna from inner circuitry. As the ground plane extends only up to about the edges of the antenna in our case (Fig. 1), the fringing fields may still interact with the circuitry, therefore a verification of robustness is needed. A common approach to analyze the robustness against the components consists in introducing a perfect-electric-conductor (PEC) object to the capsule model and analyze its effect on $|S_{11}|$ [22], [25],

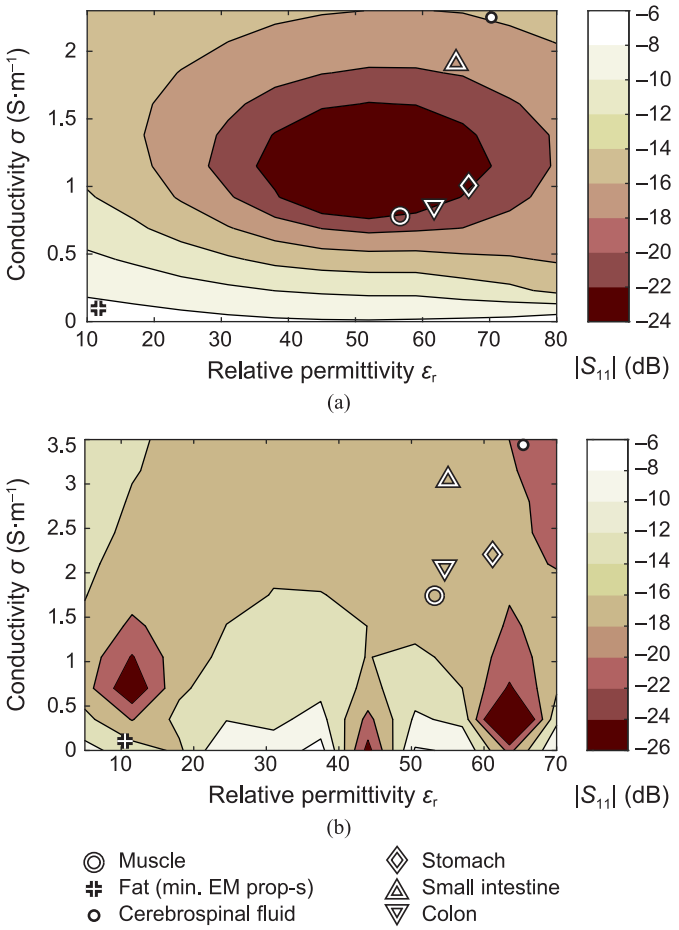

Fig. 6. Matching stability of the proposed antenna computed in a homogeneous ⌀100-mm spherical phantom within the complete range of biological tissue EM properties. (a) $|S_{11}|$ at 434 MHz for $\varepsilon_r \in [10..80]$ and $\sigma \in [0..2.4]$ S·m^{-1}. (b) $|S_{11}|$ at 2.45 GHz for $\varepsilon_r \in [5..70]$ and $\sigma \in [0..3.5]$ S·m^{-1}.

[26]. In this study, we consider the following scenario: if the components fill all available volume, how close could they be to the antenna without detuning it? For this, we: 1) introduced a PEC cylinder of a radius R_P and a length spanning the whole antenna (i.e., 19 mm) and 2) performed a parametric sweep over R_P to determine the maximum safe distance to the antenna.

For a reasonable minimal separation distance of 50-µm between the PEC cylinder and the antenna ($R_P = 3.35$ mm), only an insignificant detuning occurs. Fig. 7 compares this case with the empty capsule. The proposed antenna ensures stable impedance performance independently of the inner components of the device.

B. Radiation Performance, Reconfigurability, and SAR

Fig. 8 shows the azimuth and elevation radiation patterns of the antenna in the array and single-element states in the ⌀100 mm spherical muscle-equivalent phantom (implantation depth = 45.5 mm). The maximum realized gains G_{tot} are −28.9 dBi and −18.6 dBi, and the radiation efficiencies η equal 0.25% and 0.43% for 434 MHz and 2.45 GHz bands, respectively. Note that the gain maxima stay about the same in magnitude for both antenna states (±0.1 dBi that is comparable to a numerical error).

TABLE I
SAR (W/KG; $P_{\text{IN}} = 1$ W) AND CORRESPONDING MAXIMUM INPUT POWER LEVELS (2 W/KG 10-G SAR LIMIT [42])

	1-g SAR	10-g SAR	P_{in} (mW)	P_{in} (dBm)
434-MHz Elem.	36.9	11.8	169.5	22.3
434-MHz Array	26.7	11.5	173.9	22.4
2.45-GHz Elem.	71.0	25.0	80.0	19.0
2.45-GHz Array	58.7	24.4	82.0	19.1

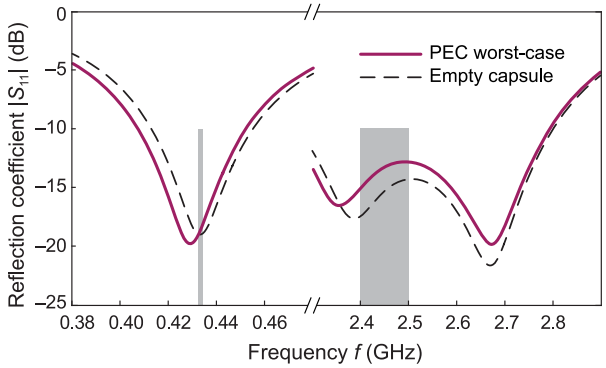

Fig. 7. Effect of capsule components on the antenna reflection coefficient. The worst-case scenario considers a PEC cylinder fully occupying the inner volume of the capsule ($R_P = 3.35$ mm).

At 434 MHz, the array has a symmetric omnidirectional short-dipole radiation pattern ($D = 1.8$ dBi) with its null oriented along the y-axis of the antenna (i.e., the elevation $\varphi = 90°$). Switching the antenna mode to a single element inclines the radiation pattern by about 15° (Fig. 8a) from the y-axis providing therefore $G_{\text{tot}} \approx -40$ dBi in the null direction of the array mode.

For the 2.45-GHz band (Fig. 8b), the directivity is increased to 4 dBi with quasi-omnidirectional radiation in the elevation plane (contrast this with the azimuth omnidirectionality at 434 MHz). At 2.45 GHz, the entire radiating structure is not electrically small, therefore the presence of higher-order modes is possible resulting in a deformation of the omnidirectional pattern. Specifically, although the main radiating element at this frequency (Z_3) operates as a $\lambda/4$ patch (Section II-B), the currents in other sections of the antenna (Fig. 2b) contribute to the total antenna near field, which defines together the quasi-omnidirectional far-field pattern in Fig. 8b.

Seeing the array configuration in Fig. 1 and knowing that the diameter of the conformal antenna is 7mm $\approx \lambda/2$ at 2.45 GHz for $\varepsilon_r = 80$, we should not be surprised to find that the radiation null is oriented along the $-z$-axis (contrast this with the $\pm y$-axis orientation of the null at 434 MHz). This pattern orthogonality of the two frequency bands can also be employed to ensure a robust communication link with the capsule.

The pattern reconfigurability at 2.45 GHz affects both azimuth and elevation patterns. In the azimuth plane, the null is rotated for about −20° when the single-element state is engaged. This enables the coverage of the $-z$ direction at $G_{\text{tot}} = -27$ dBi. Even stronger effect is observed in the

elevation plane with the radiation minimum of the array state ($G_{\text{tot}} = -28$ dBi) gaining about 5 dBi in $\varphi = 180°$ direction in the single-element state.

Using the definition of the reconfigurable gain of a capsule antenna proposed in [27] as $G_{\text{reconfig}}(\varphi, \theta) = \max(G_{\text{array}}, G_{\text{single-elem.}})$, we find that the obtained reconfigured gain has no deep nulls in both observation planes and for both operating frequencies. Moreover, since the radiation efficiency and the optimal operating frequency both strongly depend on the depth of the implant in a body [31], [32], the dual-band operation allows adjusting the operating frequency according to the device position. In general, the 434-MHz operation would be advantageous for deep-body applications (due to reduced path attenuation) whereas 2.45 GHz yields better efficiencies for the shallow one (i.e., depth $\lesssim 5$ cm) and sub-cutaneous implantation sites.

We now turn to the exposure assessment of the proposed antenna. The 2019 update of the IEEE C.95 standard limits the maximum 10-g averaged specific absorption rate (SAR) to 2 W/kg [42]. Table I summarizes the simulated 10-g SAR ($P_{\text{in}} = 1$ W) along with the corresponding maximum input power levels (1-g SAR levels are given to facilitate the comparison with prior studies). SAR is marginally higher for the single-element mode due to stronger confinement of near field in the vicinity of the antenna. In the array mode, the input power is split among two elements that spreads the power absorption over larger area, therefore reducing peak E-field and SAR. However, even for the highest considered exposure (2.45 GHz, single-element mode), P_{in} = 19.0 dBm, which is beyond the typical output power provided by miniature integrated RF power amplifiers used in implantable transceivers.

C. Radiation Efficiency vs. Fundamental Limitations

The radiation performance of in-body antennas strongly depends on how the body tissues are modeled (i.e., the phantom geometry, dimensions, and EM properties; see Section II-C), position/orientation of the device, and the size and type of the antenna [31], [32], [34]. Since it is technically impossible to decorrelate the antenna radiation from the body tissues, a direct comparison of radiation performance with counterparts (such as in Table III) should be taken with care. Ideally, an accurate comparison with counterparts requires evaluating all antennas within the same phantom configuration.

An alternative solution is to gauge the radiation performance with the maximum achievable radiation efficiency for a given antenna size in a standard, well-characterized phantom. Such fundamental limitations on the radiation efficiency of body-implanted capsules have been recently established in [31], [32] for a homogeneous spherical phantom with dispersive muscle-equivalent EM properties.

Fig. 9 benchmarks the proposed design against the maximally achievable efficiencies of corresponding optimal TM_{10} (electric) and TE_{10} (magnetic) sources in a ⌀100-mm spherical muscle-equivalent phantom computed using the methodology given in [31]. The optimal sources were calculated with the following parameters that correspond to the proposed design (units: millimeters): $L = 19$, $R = 3.5$, and $T = 1$. The

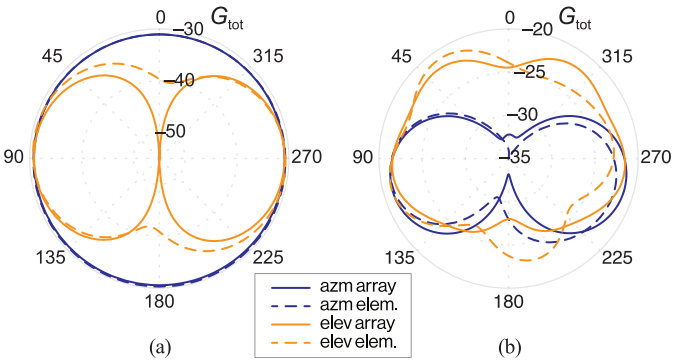

Fig. 8. 3D radiation patterns [gain G (dBi)] of the proposed antenna computed at the center of a homogeneous ⌀100-mm spherical phantom with muscle-equivalent EM properties. (a) At 434 MHz, $\max(G) = -28.9$ dBi. (b) At 2.45 GHz, $\max(G) = -18.6$ dBi.

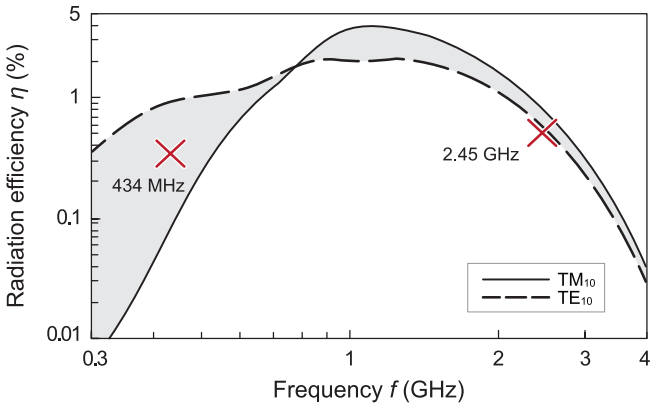

Fig. 9. Benchmark of the proposed design (red crosses) with the maximal achievable efficiencies of the ideal TM_{10} (electric) and TE_{10} (magnetic) sources in a ⌀100-mm spherical dispersive muscle-equivalent phantom. The efficiencies of the optimal sources have been calculated using the methodology given in [31].

permittivity of the source region was set to 80. Owing to the tissue-matched dielectric loading and relatively good aperture efficiency of the antenna at 434-MHz (Fig. 2a: almost entire length of the antenna contribute to the radiation), the efficiency exceeds η of a TM_{10} source.

Note that according to Fig. 9 a higher theoretical η can be achieved at 434 MHz using a TE_{10}-type (i.e., magnetic) antenna due to lower near-field losses in comparison to TM_{10}-type (electric) antennas [32]. On the other hand, the electric-type antennas benefit from dielectric loading by both the neighboring tissues and high-permittivity capsule materials, which counteracts the increased near-field losses [31], [43]. As a rule of thumb, this balance tilts towards the efficiency of electric antennas when the size is relatively large ($\gtrsim 0.5$ cm). For mm-sized implants, the magnetic antennas generally have better radiation performance [31, Fig. 3a, b].

Although for the considered phantom configuration the radiation efficiency is higher for the 2.45-GHz band, the comparison with the fundamental limitations show that the antenna is a more efficient radiating source at 434 MHz. Lower efficiency at 2.45 GHz (relative to the fundamental bounds) can be attributed to two factors: 1) less efficient antenna

aperture [Fig. 2b: note that the relatively small part of the total structure (Z_3 branch) radiates at 2.45 GHz] and 2) increased directivity (Fig. 8b) implies the existence of higher-order modes, which results in elevated power dissipation in the near field [32, Fig. 6]. Although undesirable, these factors can be seen as a required trade-off to enable the dual-band operation of the proposed antenna.

D. Impact of Capsule Shell Thickness

As the capsule shell provides a partial decoupling of the antenna from surrounding lossy tissues with varying EM properties, its thickness can affect the radiation performance in terms of both radiation and total efficiency (i.e., including $|S_{11}|$) [44]. We considered thickness $t \in [0.1, 1]$ mm to quantify the its effect on the performance of the antenna. The numerical results in Fig. 10a show that the radiation efficiency η is linearly proportional to t for both frequencies over the considered range. A strong effect of t at 2.45 GHz can be attributed to the radiation of higher-order modes, which results in larger power dissipation in the near field [32].

Fig. 10b shows the effect of t on $|S_{11}|$. The effect is stronger at 434 MHz due to the narrower BW compared to the 2.45-GHz band (Fig. 3) The antenna, however, remains well matched ($|S_{11}| < -10$ dB) for both bands within the considered range of t. This performance stability is mainly attributed to the tissue-matched dielectric loading of the antenna and also to the fact that we deal with a lossy medium that intrinsically increases BW.

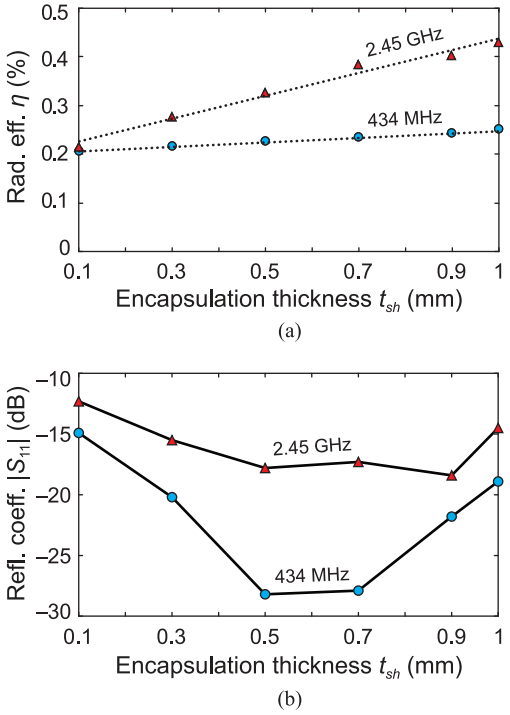

Fig. 10. Effect of the encapsulation thickness on antenna performance: (a) radiation efficiency η and (b) reflection coefficient $|S_{11}|$ at 434 MHz and 2.45 GHz.

IV. Measurements

A. Prototyping and Phantoms

The antenna array prototype was printed on a 101.6-µm-thick (4 mil) Rogers ULTRALAM 3850HT substrate with 9-µm copper thickness using the laser ablation method (LPKF ProtoLaser S). Although this technique provides fast and relatively accurate prototyping, it does not allow through-substrate connections using vias. To overcome this issue, we used an array configuration of the proposed antenna to validate the numerical results. This helped avoiding a via in the switch location. Furthermore, in order to ground the Z_2 elements without a via, we manually folded them over the edge of the substrate and soldered to the ground plane as shown in Fig. 11a. The resulted antenna was soldered to a 100-mm-long 50-Ω semi-rigid coaxial cable feed terminated with an SMA connector. Next, the substrate was rolled and inserted into a 28 mm × ⌀9 mm ceramic shell (TCI Ceramics "K-80" [45], $\varepsilon_r \approx 80 \ \forall \ f_{\mathrm{op}}$); such EM properties are characteristic to perovskite materials [46] (barium/calcium titanates in our case). The feed-side opening was sealed using the Araldite 2011 epoxy glue (Fig. 11b). Next, the capsule was filled with pure water, outgassed, and closed at the opposite opening with a rubber plug. Pure water has $\varepsilon_r \sim 80$ and therefore provides wave-impedance matching through the gap between the antenna and the superstrate for consistent dielectric loading. Note that water is used here as a technical proof of concept for ensuring reliable measurements (otherwise, the air gap between the antenna and the superstrate will hinder the antenna performance). For industrial applications of the proposed design, a more scalable, reliable, and economical approach would be to glue the antenna to the shell from the inside using a very thin (< 5 µm) layer of a bonding polymer with an application of the force from the inside (e.g., using an inflatable actuator) in an outgassing environment. Considering

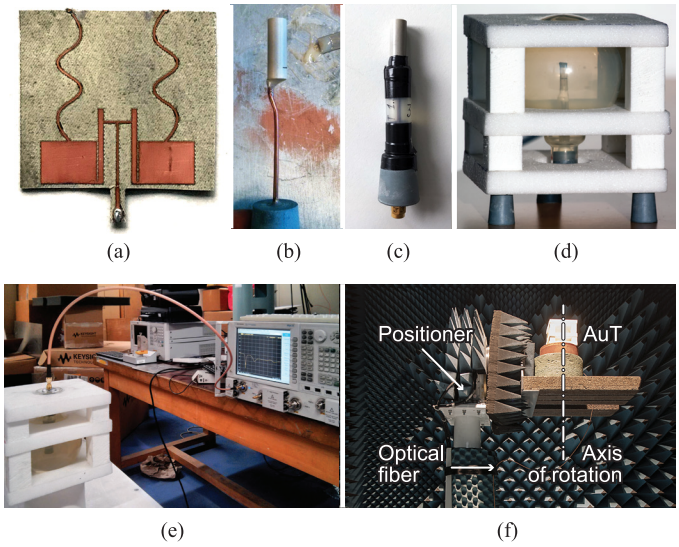

Fig. 11. Prototyping steps and measurement setup. (a) Planar array shaped on a Rogers ULTRALAM 3850HT substrate. (b) Antenna soldered to a semi-rigid coaxial cable, inserted into the ceramic shell, and sealed with epoxy. (c) Fully assembled prototype of AuT including an airtight tube to partially decouple the coaxial feed from the antenna when measured in phantoms. (d) AuT placement example inside of a ⌀100-mm spherical container. (e) Impedance characterization setup. (f) Far-field characterization setup in the IETR cm-wave anechoic chamber using a fiber-optic feed (detailed outline in Fig. 14).

TABLE II
WATER–SUCROSE–NACL PHANTOMS USED FOR MEASUREMENTS: TARGET EM PROPERTIES AND CONCENTRATIONS

	434 MHz	**2.45 GHz**
Relative permittivity ε_r	56.9	52.7
Conductivity σ (S·m^{-1})	0.8	1.7
Concentration of sucrose (%)	51.3	41.8
Concentration of NaCl (%)	1.53	0

the operating frequency, a µm-thick low-loss bonding layer with its permittivity close to the substrate ($\varepsilon_r \sim 3$) will have only an insignificant effect on the antenna $|S_{11}|$ that can be accounted for during fine-tuning of the finalized design.

To characterize the prototype in terms of impedance and radiation, we prepared two liquid muscle-equivalent phantoms (one for each frequency band). We used a water–sugar–salt formula [47], [48] to achieve the target EM properties. Pure deionized water was the base component of the phantom, sucrose ($C_{12}H_{22}O_{11}$, Sigma-Aldrich "BioXtra Sucrose," S7903, $\geq 99.5\%$) reduced the permittivity ε_r, and sodium chloride (NaCl, Sigma-Aldrich "BioXtra Sodium Chloride," S7653, $\geq 99.5\%$) increased the conductivity σ (for 434 MHz only). Table II gives the target EM properties along with the recipes of the phantoms used in this study. The liquid phantoms were prepared and characterized in a temperature-controlled room (25 ± 0.5 °C). The weighting precision was $\pm 0.01\%$ (Kern precision balance EMB 2000-2). To validate the EM properties of the obtained phantoms, we used a SPEAG DAK kit with DAK-12 probe [49]. Fig. 12 compares the achieved EM properties of the phantoms with the target ones. The discrepancy at 2.45 GHz is attributed to the difficulty of reducing the loss to the target value at this frequency using the water–sucrose formula. Reducing the sucrose concentration might slightly improve the agreement. However, considering the robust characteristics of the antenna (Fig. 6), the achieved EM properties are adequate for both bands.

To contain the liquid phantom for antenna measurements, we used a ⌀100-mm spherical glass jar (Fig. 11d)—the same shape and dimensions that we defined for the canonical computational phantom earlier. Rohacell IG foam frame ($\varepsilon_r = 1.05, \tan\delta = 0.0017$) secures the phantom for accurate positioning in an anechoic chamber. To help decoupling the antenna from the feed, we applied the methodology proposed by Merli *et al.* [22] consisting in insulating the feed from the phantom by an air layer. For that, we used a ⌀12-mm polyamide tube sealed with silicone to isolate the feeding cable from the phantom (Fig. 11c). The tube terminates with a rubber plug that seals the spherical jar. In this way, the SMA connector remains outside of the watertight jar easing the connection of the antenna under test to measurement equipment (AuT, Fig. 11e–f).

B. Reflection Coefficient

An Agilent PNA-X vector network analyzer (VNA) was used to measure the antenna reflection coefficient. Fig. 11e shows the measurement setup. Since the post-calibration reference plane locates at the SMA connector outside of the phantom, a de-embedding was required. For this, the results were post-processed in CST Design Studio to de-embed the effect of the cable on antenna impedance.

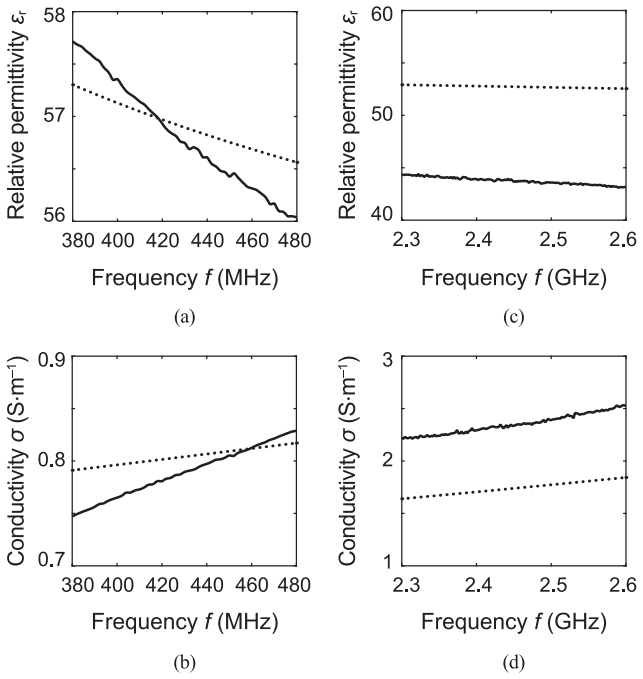

Fig. 12. Measured (—) and target ($\cdots$) EM properties (ε_r, σ at 25 ± 0.5 °C) of the liquid phantoms. (a, b) At 434 MHz. (c, d) At 2.45 GHz.

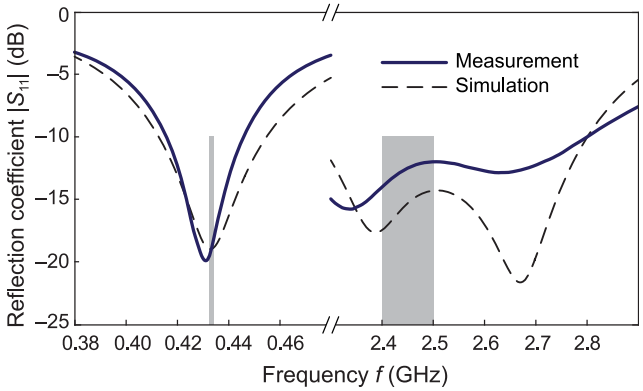

Fig. 13. Measured and computed reflection coefficients $|S_{11}|$ of the proposed antenna in phantoms with EM properties close to muscle (Fig. 12).

Fig. 13 shows the reflection coefficients $|S_{11}|$ of the fabricated antenna prototype as measured in two phantoms (Table II). The experimental results agree fairly well with the simulations. The discrepancy—especially, for the 2.45 GHz band—can be attributed to the manufacturing method (the laser ablation provides lower precision than, for instance, photolithography), to the minor coupling to the feeding cable (the technique that we used does not fully decouple the antenna, and the cable modes can also affect the results [22]). The measured results show, however, that the antenna operates as intended having a resonance at 434 MHz and a double-resonance around 2.45 GHz.

C. Radiation Performance

Considering the miniature dimensions of capsule antennas and their radiation efficiencies $\eta \lesssim 1\%$ due to losses in tissues/phantoms, accurate characterization of the radiation performance is nontrivial [50]. To address this challenge, we use a combined approach consisting of a far-field direct illumination of the AuT placed in a fully-anechoic chamber and fed with an electro-optical converter (enprobe LFA-3 [51]). Fig. 14 outlines the methodology. AuT is placed at the distance $d = 3$ m from the measurement horn fulfilling the far-field criterion $d > 2\lambda$. The radiation was measured in the azimuth plane (elevation $\varphi = 0°$), for both co- and cross-polarization components. To derive the realized gain from the measured data, we used a gain substitution technique. Specifically, a reference antenna of a known gain (ETS-Lindgren open-boundary quad-ridged horn 3164-06 [52], $G_{434} = 4.5$ dBi, $G_{2.45} = 9$ dBi) was used. The measured gain of the reference antenna was used to calibrate the AuT results. Fig. 15 shows the far-field characterization results. The maximum realized gains G_{tot} in the azimuthal plane are -29.3 dBi and -22.1 dBi for 434 MHz and 2.45 GHz, respectively. Due to the positioner tower angle limitations (see [9]), measurement artifacts are produced within the angular range $\theta \in [110°, 250°]$. Within the remaining angular range, the radiation patterns and maximum gain values are in close agreement with the simulated ones.

Table III compares the proposed antenna with relevant counterparts (multi-band and reconfigurable capsule-conformal antennas). The reader is warned that the gain values are listed for completeness, and that the direct comparison is inaccurate since it requires analyzing all antennas within the same phantom configuration. In addition, the maximum achievable radiation efficiency (and therefore the gain) strongly depends on the antenna dimensions. For more information on this topic, the reader is invited to look in [31], [32].

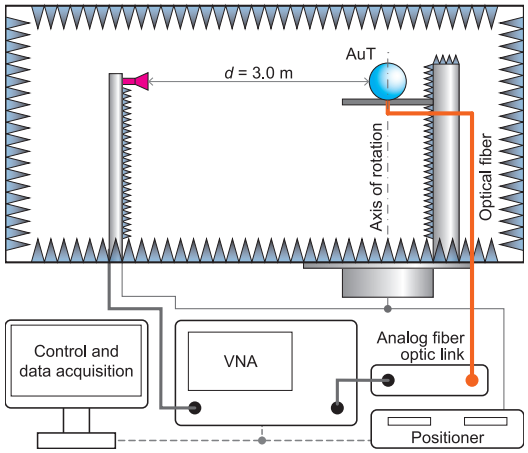

Fig. 14. Outline of the far-field measurement setup in the cm-wave anechoic chamber of IETR using an analog fiber-optic link.

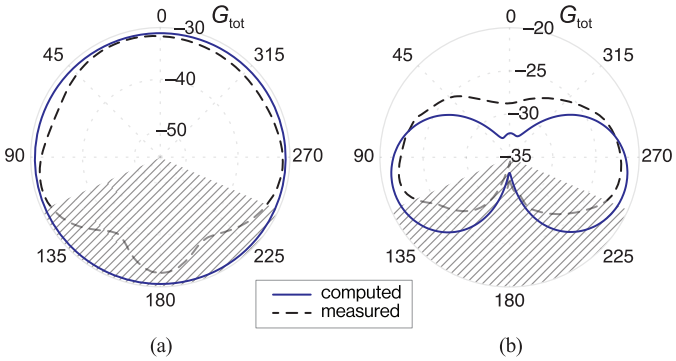

Fig. 15. Measured and computed far-field azimuthal radiation patterns of the antenna centered in a ⌀100-mm spherical phantom with EM properties close to muscle (Fig. 12) at (a) 434 MHz and (b) 2.45 GHz. 0°-bearing aligns with the z-axis (the axes are defined in Fig. 1). The shaded area denotes the angular range where the tower positioner causes the shadowing effect (Fig. 11f).

V. Conclusion

This study proposed a pattern-reconfigurable dual-band antenna array that can be used for versatile in-body capsule applications. The design approach was based on the theoretical findings [31] that predicted more efficient operation of tissue-matched (i.e., real part of the capsule shell permittivity is matched with water-based tissues) electric-type in-body antennas compared to the magnetic ones. Owing to good aperture efficiency of the antenna that was further improved by dielectric loading, the obtained radiation efficiency is close to the fundamental limitations (established for an ideal source of the same dimensions). Choosing a microstrip-based design among other electric-type antennas improves the antenna versatility as it features an integral ground plane. It shields the conformal antenna from the capsule payload and has a double benefit of improving the EM compatibility and making the antenna impedance independent of the configuration of inner components (e.g., batteries, circuits, and sensors). Dual-band operation allows adjusting the operating frequency to ensure efficient transmission/reception of EM energy for both shallow and deep-body implantations. For both operating bands, the antenna remains well-matched for the majority of body tissues that further improves its versatility.

Finally, the antenna reconfigurability enables a synthetic null-free radiation pattern mitigating the uncertainty of the antenna position and orientation in a body. A cautionary remark: the proposed reconfigurability approach requires a DC power source and a microcontroller to actuate the switch. Although most capsule-sized in-body devices already contain an MCU and batteries [1], an additional MCU channel/pin must be allocated to operate the switch. As for the power consumption of a typical CMOS-switch (about –25 dBm), it is negligible in comparison to the $\sim$ 10..20 dBm power consumed by the antenna. Therefore, the ability to fill antenna nulls is clinically significant to avoid missing data from potentially abnormal regions.

References

[1] E. Katz, *Implantable Bioelectronics*. Weinheim, Germany: Wiley, 2014.
[2] A. Kiourti and K. S. Nikita, "A review of in-body biotelemetry devices: implantables, ingestibles, and injectables," *IEEE Trans. Biomed. Eng.*, vol. 64, no. 7, pp. 1422–1430, Jul. 2017.
[3] J. J. Jun *et al.*, "Fully integrated silicon probes for high-density recording of neural activity," *Nature*, vol. 551, no. 7679, pp. 232–236, Nov. 2017.
[4] K. Famm, B. Litt, K. J. Tracey, E. S. Boyden, and M. Slaoui, "Drug discovery: A jump-start for electroceuticals," *Nature*, vol. 496, pp. 159–161, Apr. 2013.

TABLE III
COMPARISON OF THE MULTI-BAND OR RECONFIGURABLE IN-BODY CAPSULE ANTENNAS REPORTED IN LITERATURE

Ref.	**Antenna type**	**Capsule** (mm)	f_0 (MHz)	G (dBi)	Reconfigurability	**Phantom: tissue, shape, size** (mm)
This work	Microstrip	$28 \times \varnothing 9$	434 2450	-28.9 -18.6	Pattern	Muscle, sphere, $\varnothing 100$
[18]	Microstrip	$26 \times \varnothing 11$	402 915 1200	-30.8 -19.7 -18.7		Muscle, cuboid, $20 \times 100 \times 100$
[21]	Meandered loop	$26 \times \varnothing 11$	402 915 2450	-27.6 -23.6 -15.7		Muscle, cube, 200^3
[22]	Multilayer spiral	$32 \times \varnothing 10$	403 2450	-28.8 -18.5		Muscle, cylinder*, $110 \times \varnothing 80$
[23]	Loop + RIS	$10 \times \varnothing 5$	920 2450	-29.3 -21.0		Skin, cube, 5^3
[24]	Patch	$26 \times \varnothing 11$	915 2450	-28.2 -24.5		Muscle, cube, 100^3
[25]	Loop w/ CSRR	$25 \times \varnothing 10$	434 2450	-25.1 -15.0		Mus., ellip. cyl., $50 \times \varnothing 180 \times \varnothing 100$
[26]	Inverted-F	$32 \times \varnothing 10$	403 915 2450	-29.7 -24.9 -23.2		Stomach, anatomical (Gustav)†
[27]	Dipole + loop	$26 \times \varnothing 11$	2450	-24.1	Pattern	Muscle, cuboid, $60 \times 60 \times 70$

* The capsule is off-centered, distance to the surface ≈ 10 mm.
† The distance to the surface is 5.5 cm.

[5] G. L. Barbruni, P. M. Ros, D. Demarchi, S. Carrara, and D. Ghezzi, "Miniaturised wireless power transfer systems for neurostimulation: A review," *IEEE Trans. Biomed. Circuits Syst.*, vol. 14, no. 6, pp. 1160–1178, Dec. 2020.

[6] S. Ma, T. Bjorninen, L. Sydanheimo, M. H. Voutilainen, and L. Ukkonen, "Double split rings as extremely small and tuneable antennas for brain implantable wireless medical microsystems," *IEEE Trans. Antennas Propagat.*, vol. 69, no. 2, pp. 760–768, Feb. 2021.

[7] M. K. Magill, G. A. Conway, and W. G. Scanlon, "Tissue-independent implantable antenna for in-body communications at 2.36–2.5 GHz," *IEEE Trans. Antennas Propag.*, vol. 65, no. 9, pp. 4406–4417, Sep. 2017.

[8] K. Zhang *et al.*, "A conformal differentially fed antenna for ingestible capsule system," *IEEE Trans. Antennas Propag.*, vol. 66, no. 4, pp. 1695–1703, Apr. 2018.

[9] D. Nikolayev, M. Zhadobov, L. Le Coq, P. Karban, and R. Sauleau, "Robust ultra-miniature capsule antenna for ingestible and implantable applications," *IEEE Trans. Antennas Propag.*, vol. 65, no. 11, pp. 6107–6119, Nov. 2017.

[10] A. Khaleghi, A. Hasanvand, and I. Balasingham, "Radio frequency backscatter communication for high data rate deep implants," *IEEE Trans. Microwave Theory Techn.*, vol. 67, no. 3, pp. 1093–1106, Mar. 2019.

[11] Z. Duan, L. J. Xu, S. Gao, and W. Geyi, "Integrated design of wideband omnidirectional antenna and electronic components for wireless capsule endoscopy systems," *IEEE Access*, vol. 6, pp. 29626–29636, May 2018.

[12] T. Dissanayake, K. P. Esselle, and M. R. Yuce, "Dielectric loaded impedance matching for wideband implanted antennas," *IEEE Trans. Microw. Theory Tech.*, vol. 57, no. 10, pp. 2480–2487, Oct. 2009.

[13] Y. Fan, J. Huang, T. Chang, and X. Liu, "A miniaturized four-element MIMO antenna with EBG for implantable medical devices," *IEEE J. Electromagn. RF Microw. Med. Biol.*, vol. 2, no. 4, pp. 226–233, Dec. 2018.

[14] S. Xiao, C. Liu, Y. Li, X. M. Yang, and X. Liu, "Small-size dual-antenna implantable system for biotelemetry Devices," *IEEE Antenn. Wireless Propag. Lett.*, vol. 15, pp. 1723–1726, Feb. 2016.

[15] Z. Bao and Y.-X. Guo, "Novel miniaturized antenna with a highly-tunable complex input impedance for capsules," *IEEE Trans. Antennas Propagat.*, accepted, doi: 10.1109/TAP.2020.3037762

[16] D. Nikolayev, M. Zhadobov, and R. Sauleau, "Immune-to-detuning wireless in-body platform for versatile biotelemetry applications," *IEEE Trans. Biomed. Circuits Syst.*, vol. 13, no. 2, pp. 403–412, Apr. 2019.

[17] Y. Peng, K. Saito, and K. Ito, "Antenna design for impulse-radio-based wireless capsule endoscope communication systems," *IEEE Trans. Antennas Propag.*, vol. 66, no. 10, pp. 5031–5042, Oct. 2018.

[18] M. Yousaf *et al.*, "Compacted conformal implantable antenna with multitasking capabilities for ingestible capsule endoscope," *IEEE Access*, vol. 8, pp. 157617–157627, Aug. 2020.

[19] L.-J. Xu, Y.-X. Guo, and W. Wu, "Miniaturized dual-band antenna for implantable wireless communications," *IEEE Antennas Wireless Propag. Lett.*, vol. 13, pp. 1160–1163, 2014.

[20] Y. Liu, Y. Chen, H. Lin, and F. Juwono, "A novel differentially fed compact dual-band implantable antenna for biotelemetry applications", *IEEE Antennas Wireless Propag. Lett.*, vol. 15, pp. 1791–1794, 2016.

[21] A. Basir, M. Zada, Y. Cho, and H. Yoo, "A dual-circular-polarized endoscopic antenna with wideband characteristics and wireless biotelemetric link characterization," *IEEE Trans. Antennas Propag.*, vol. 68, no. 10, pp. 6953–6963, Oct. 2020.

[22] F. Merli, L. Bolomey, J.-F. Zurcher, G. Corradini, E. Meurville, and A. K. Skrivervik, "Design, realization and measurements of a miniature antenna for implantable wireless communication systems," *IEEE Trans. Antennas Propag.*, vol. 59, no. 10, pp. 3544–3555, Oct. 2011.

[23] G. Samanta and D. Mitra, "Dual-band circular polarized flexible implantable antenna using reactive impedance substrate," *IEEE Trans. Antennas Propagat.*, vol. 67, no. 6, pp. 4218–4223, Jun. 2019.

[24] S. Hayat, S. A. A. Shah, and H. Yoo, "Miniaturized dual-band circularly polarized implantable antenna for capsule endoscopic system," *IEEE Trans. Antennas Propagat.*, accepted, doi: 10.1109/TAP.2020.3026881

[25] R. Alrawashdeh, Y. Huang, M. Kod, and A. Sajak, "A broadband flexible implantable loop antenna with complementary split ring resonators," *IEEE Antennas Wirel. Propag. Lett.*, vol. 14, pp. 1506–1509, 2015.

[26] Z. Bao, Y.-X. Guo, and R. Mittra, "Single-layer dual-/tri-band inverted-F antennas for conformal capsule type of applications," *IEEE Trans. Antennas Propag.*, vol. 65, no. 12, pp. 7257–7265, Sep. 2017.

[27] Z. Bao, Y.-X. Guo, and R. Mittra, "Conformal capsule antenna with reconfigurable radiation pattern for robust communications," *IEEE Trans. Antennas Propag.*, vol. 66, no. 7, pp. 3354–3365, Apr. 2018.

[28] K. L.-L. Roman, G. Vermeeren, A. Thielens, W. Joseph, and L. Martens, "Characterization of path loss and absorption for a wireless radio frequency link between an in-body endoscopy capsule and a receiver

outside the body," *J. Wireless Com. Network*, vol. 2014, no. 1, pp. 1–10, Feb. 2014.
[29] S. Benaissa *et al.*, "Propagation-loss characterization for livestock implantables at 433, 868, and 1400 MHz," *IEEE Trans. Antennas Propag.*, vol. 69, no. 8, pp. 5166–5170, Aug. 2021.
[30] D. Nikolayev, M. Zhadobov, P. Karban, and R. Sauleau, "Electromagnetic radiation efficiency of body-implanted devices," *Phys. Rev. Appl.*, vol. 9, no. 2, pp. 024033, Feb. 2018.
[31] D. Nikolayev, W. Joseph, M. Zhadobov, R. Sauleau, and L. Martens, "Optimal radiation of body-implanted capsules," *Phys. Rev. Lett.*, vol. 122, no. 10, p. 108101, Mar. 2019.
[32] A. K. Skrivervik, M. Bosiljevac, and Z. Sipus, "Fundamental limits for implanted antennas: Maximum power density reaching free space," *IEEE Trans. Antennas Propag.*, vol. 67, no. 8, pp. 4978–4988, Aug. 2019.
[33] D. Nikolayev, W. Joseph, A. K. Skrivervik, M. Zhadobov, L. Martens, and R. Sauleau, "Dielectric-loaded conformal microstrip antennas for versatile in-body applications," *IEEE Antenn. Wireless Propag. Lett.*, vol. 18, no. 12, pp. 2686–2690, Dec. 2019.
[34] D. Nikolayev, M. Zhadobov, and R. Sauleau, "Impact of tissue electromagnetic properties on radiation performance of in-body antennas," *IEEE Antenn. Wireless Propag. Lett.*, vol. 17, no. 8, Jun. 2018.
[35] S. Gabriel, R. W. Lau, and C. Gabriel, "The dielectric properties of biological tissues: II. Measurements in the frequency range 10 Hz to 20 GHz," *Phys. Med. Biol.*, vol. 41, pp. 2251–2269, Nov. 1996.
[36] D. M. Pozar, *Microwave Engineering*, 4th ed. Hoboken, NJ: John Wiley & Sons, 2012.
[37] D. Nikolayev, M. Zhadobov, P. Karban, and R. Sauleau, "434 MHz ISM band antenna for in-body biotelemetry capsules," in *Proc. 11th Eur. Conf. Antennas and Propagation (EuCAP 2017)*, Paris, France, Mar. 2017, pp. 1035–1038.
[38] C. A. Balanis, *Antenna Theory: Analysis and Design*, 4th ed. Hoboken, NJ: John Wiley & Sons, 2016.
[39] D. Nikolayev, Z. Kubik, P. Karban, and J. Skala, "Impedance analysis of transmission line cells for EMC applications using Agros2D," *Appl. Math. Comput.*, vol. 289, pp. 381–387, Oct. 2016.
[40] R. Moore, "Effects of a surrounding conducting medium on antenna analysis," *IEEE Trans. Antennas Propagat.*, vol. 11, no. 3, pp. 216–225, May 1963.
[41] Dassault Systèmes. *CST Studio Suite*. Accessed: Feb. 20, 2021. [Online]. Available: https://www.3ds.com/products-services/simulia/products/cst-studio-suite/
[42] "*IEEE Standard for Safety Levels with Respect to Human Exposure to Electric, Magnetic and Electromagnetic Fields, 0 Hz to 300 GHz*," IEEE Standard C95.1-2019, 2019.
[43] D. Nikolayev, W. Joseph, R. Sauleau, M. Zhadobov, L. Martens, and A. K. Skrivervik, "Influence of body-implanted capsule dimensions and materials on achievable radiation efficiency," in *Proc. Asia-Pacific Microwave Conf. (APMC 2019)*, Singapore, Dec. 2019.
[44] F. Merli, B. Fuchs, J. R. Mosig, and A. K. Skrivervik, "The effect of insulating layers on the performance of implanted antennas," *IEEE Trans. Antennas Propag.*, vol. 59, no. 1, pp. 21–31, Jan. 2011.
[45] TCI Ceramics. *K-80*. Accessed: Feb. 20, 2021. [Online]. Available: http://www.magneticsgroup.com/m_dielec.htm
[46] M. T. Sebastian, *Dielectric Materials for Wireless Communication*. Oxford, UK: Elsevier, 2010.
[47] P. Hall and Y. Hao, *Antennas and Propagation for Body-Centric Wireless Communications*, 2nd Edition. Norwood, MA: Artech House, 2012.
[48] T. Karacolak, A. Hood, and E. Topsakal, "Design of a dual-band implantable antenna and development of skin mimicking gels for continuous glucose monitoring," *IEEE Trans. Microw. Theory Tech.*, vol. 56, no. 4, pp. 1001–1008, Apr. 2008.
[49] Schmid & Partner Engineering AG. *Dielectric Assessment Kit*. Accessed: Feb. 20, 2021. [Online]. Available: http://www.speag.com/products/dak/dielectric-measurements
[50] L. Huitema, C. Delaveaud, and R. D'Errico, "Impedance and radiation measurement methodology for ultra miniature antennas," *IEEE Trans. Antennas Propag.*, vol. 62, no. 7, pp. 3463–3473, Jul. 2014.
[51] enprobe GmbH. *LFA-3 Analog Fiber Optic Link*. Accessed: Feb. 20, 2021. [Online]. Available: http://www.enprobe.de/products_FO-Links.htm
[52] ETS-Lindgren. *3164-06 Open Boundary Quad-Ridged Horn*. Accessed: Feb. 20, 2021. [Online]. Available: http://www.ets-lindgren.com/products/antennas/open-boundary-quad-ridged-horn/4003/400303

Denys Nikolayev (S'14–M'17) received the M.Sc. (*summa cum laude*) degree in Radiophysics from the Lviv Polytechnic National University, Ukraine, in 2008, and the Ph.D. degrees in Electronics from the University of Rennes 1, France, and in Electrical Engineering from the University of West Bohemia, Czechia, in 2017.

He was a Postdoctoral Fellow with the Imec / Ghent University, Belgium until 2018, a Scientist at École polytechnique fédérale de Lausanne (EPFL) until 2020, and then joined the French National Center for Scientific Research (CNRS) as a tenured Senior Researcher (chargé de recherche). His research interests are centered on theoretical foundations and engineering of wireless bioelectronics, biosensors, and electroceuticals.

Dr. Nikolayev received Best Ph.D. Dissertation Award by the Foundation Rennes One. He is a laureate of the Eiffel Excellence Doctoral Fellowship (2015–16). He received the Young Scientist Award at EMBEC/NBC 2017 and Student Awards at BioEM 2015 and URSI-France 2017. He is a co-recipient of the ANR–NRF PRCI Research Fellowship (2021; Agence nationale de la recherche, France, and National Research Foundation, Singapore).

Anja K. Skrivervik received the master's degree in electrical engineering and the Ph.D. degree from the Ecole Polytechnique Fédérale de Lausanne (EPFL), Lausanne, Switzerland, in 1986 and 1992, respectively.

She was an Invited Research Fellow with the University of Rennes 1, Rennes, France, followed by two years in the industry. In 1996, she rejoined EPFL, as an Assistant Professor, where she is currently a Full Professor and also the Head of the Microwave and Antenna Group. She was the Director of the EE Teaching Section, EPFL, from 1996 to 2000. She is currently the Director of the Electrical Engineering Doctoral School, EPFL. Her teaching activities include courses on microwaves and antennas and courses at bachelor's, master's, and Ph.D. levels. She has authored or co-authored over 200 peer-reviewed scientific publications. Her current research interests include electrically small antennas, antennas in biological media, multifrequency and ultrawideband antennas, and numerical techniques for electromagnetics.

Prof. Skrivervik has been a member of the Board of Directors of the European Association on Antennas and Propagation, since 2017. She is a Board Member of the European School on Antennas. She received the Latsis Award for her Ph.D. thesis from EPFL. She is frequently requested to review research programs and centers in Europe. She was the Chairperson of the Swiss URSI until 2012.

John S. Ho (M'15) received the Ph.D. degree in electrical engineering from Stanford University, Stanford, CA, USA in 2015. He is currently an Assistant Professor with the Department of Electrical and Computer Engineering and the Department of Biomedical Engineering (by courtesy) at the National University of Singapore (NUS), Singapore. His research interests are centered on the development and translation of wireless technologies for bioelectronic devices.

He was a National Defense Science and Engineering Graduate Fellow (2012–2015) at Stanford University. He is a recipient of the NUS Young Investigator Award (2016), National Research Foundation Fellowship (2017), MIT Technology Review Innovator Under 35 Asia (2017), and Singapore Young Scientist Award (2020).

Maxim Zhadobov (S'05–M'07–SM'15) received the Ph.D. degree from the IETR (Institut d'Electronique et des Technologies du numeRique), University of Rennes 1, France, in 2006. He was a Postdoctoral Researcher with the Center for Biomedical Physics, Temple University, Philadelphia, PA, USA, until 2008, and then joined the French National Center for Scientific Research (CNRS).

He is currently the Senior Research Scientist at the IETR/CNRS and head of the WAVES research team, IETR. His scientific interests and research activities are in the field of innovative biomedical applications of electromagnetic fields and associated technologies. He coauthored 5 book chapters, more than 80 research papers in peer-reviewed international journals and 200 contributions to conferences and workshops. His review article in the Int. J. Microwave Wireless Techn. has been the most cited paper in 2016–2020. A paper published by his research group in 2019 is in Journal Top 100 of Nature Scientific Reports. He has been involved in 25 research projects (12 as PI).

Dr. Zhadobov was the TPC co-chair of BioEM 2021 and BioEM 2020. He was a TPC member and / or session organizer at international conferences, including IEEE IMBioC 2022, AT-AP-RASC 2022, BioEM 2019, EuMW 2019, IEEE iWEM 2017, MobiHealth 2015-2017, BodyNets 2016, and IMWS-Bio 2014. He is an elected member of EBEA Council, member of IEEE TC95.4, and vice-president of URSI France Commission K. He is Associate Editor of IEEE Journal of Electromagnetics RF and Microwaves in Medicine and Biology and served as a guest editor of several special issues, including "Human Exposure in 5G and 6G Scenarios" of Applied Sciences. He is a member of the Technical Advisory Committee URSI Com-K and has been acting as an expert at research councils worldwide. He received CNRS Medal in 2018, EBEA Award for Excellence in Bioelectromagnetics in 2015, and Brittany's Young Scientist Award in 2010.

Ronan Sauleau (M'04–SM'06–F'18) graduated in electrical engineering and radio communications from the Institut National des Sciences Appliquées, Rennes, France, in 1995. He received the Agrégation degree from the Ecole Normale Supérieure de Cachan, France, in 1996, and the Doctoral degree in signal processing and telecommunications and the "Habilitation à Diriger des Recherches" degree, both from the University of Rennes 1, France, in 1999 and 2005, respectively.

He was an Assistant Professor and Associate Professor at the University of Rennes 1, between Sept. 2000 and Nov. 2005, and between Dec. 2005 and Oct. 2009, respectively. He has been appointed as a full Professor in the same University since Nov. 2009. His current research fields are numerical modeling, millimeter-wave printed and reconfigurable (MEMS) antennas, substrate integrated waveguide antennas, lens-based focusing devices, periodic and non-periodic structures (electromagnetic bandgap materials, metamaterials, reflectarrays, and transmitarrays), and biological effects of millimeter waves. He has been involved in more than 70 research projects at the national and European levels and has co-supervised 27 post-doctoral fellows, 53 PhD students and 50 master students.

He has received 20 patents and is the author or coauthor of more than 270 journal papers and 560 publications in international conferences and workshops. He shared the responsibility of the research activities on antennas at IETR in 2010 and 2011. He was co-director of the research Department 'Antenna and Microwave Devices' at IETR and deputy director of IETR between 2012 and 2016. He is now director of IETR. Prof. Sauleau received the 2004 ISAP Conference Young Researcher Scientist Fellowship (Japan) and the first Young Researcher Prize in Brittany, France, in 2001 for his research work on gain-enhanced Fabry-Perot antennas. In Sep. 2007, he was elevated to Junior member of the "Institut Universitaire de France." He was awarded the Bronze medal by CNRS in 2008 and the silver medal in 2020. He received the 2021 Antenna EurAAP Award. He was a co-recipient of several international conference awards with his students (BioEM'2005, BEMS'2006, MRRS'2008, E-MRS'2011, BEMS'2011, IMS'2012, Antem'2012, BioEM'2015, EuCAP'2019, EuCAP'2021). He served as a guest editor for IEEE Antennas Propog. Special Issue on "Antennas and Propagation at mm and sub mm waves". He served as a national delegate for several EU COST actions. He has served as a national delegate for EurAAP and as a member of the board of Director of EurAAP from 2013 to 2018.